

Supporting Information for

# The Role of Gain in Fabry–Pérot Surface Plasmon Polariton Lasers

*Marianne Aellen<sup>†</sup>, Aurelio A. Rossinelli<sup>†</sup>, Robert C. Keitel<sup>†</sup>, Raphael Brechbühler<sup>†</sup>,  
Felipe V. Antolinez<sup>‡</sup>, Sergio G. Rodrigo<sup>‡,§</sup>, Jian Cui<sup>†,||</sup>, and David J. Norris<sup>†,\*</sup>*

<sup>†</sup>Optical Materials Engineering Laboratory, Department of Mechanical and Process Engineering,  
ETH Zurich, 8092 Zurich, Switzerland

<sup>‡</sup>Departamento de Física Aplicada, Facultad de Ciencias, Universidad de Zaragoza, 50009 Zaragoza, Spain

<sup>§</sup>Instituto de Nanociencia y Materiales de Aragón (INMA), CSIC-Universidad de Zaragoza, 50009 Zaragoza, Spain

<sup>||</sup>Helmholtz Pioneer Campus, Helmholtz Zentrum München, 85764 Neuherberg, Germany

## Contents

**Section S1. Temperature Dependence**

**Section S2. Major Loss Channels**

**Section S3. Lasing Condition**

**Section S4. Estimation of Mirror Reflectivity of Ag Reflectors**

**Section S5. Confinement Factor, Propagation Length, and Threshold Gain**

**Section S6. Gap-Layer Design Criteria**

**Section S7. Inflection Strength of Light–Light Curve at Threshold**

**Section S8. Spontaneous-Emission-Factor Calculation**

**Section S9. Effect of Mirror Reflectivity on Lasing Mode**

**Section S10. Fabrication of Laser Cavities**

**Section S11. Optical Characterization**

**Section S12. Multilayer-Waveguide Model**

**Section S13. Ellipsometry of NPL, Ag, and Alumina Films**

**Section S14. Waveguide Dispersion**

**Section S15. Laser Rate Equations**

**Section S16. Fraction of Absorbed Pump Power**

**Section S17. Material Gain Estimation for Rate-Equation Model**

**Section S18. Mode-Switching Discussion**

**Section S19. Supplementary References**

## Section S1. Temperature Dependence

We have probed our devices at various temperatures ranging from 4 K to room temperature. With increasing temperature, devices with thinner gain layers stopped lasing (Figure S1). At 100 K, devices thicker than the photonic-mode cutoff thickness were still displaying lasing in the photonic mode, while only the device with the thickest gain layer below the photonic-mode cutoff thickness (device with  $d_{\text{NPL}} = 66$  nm) was able to lase in the plasmonic mode (Figure S1c). At room temperature, only the device with the thickest gain layer ( $d_{\text{NPL}} = 85$  nm) displayed photonic lasing (Figure S1d). It has been reported that the optical-gain threshold for colloidal NPLs is reduced at cryogenic temperatures.<sup>S1</sup> We believe that in our metallic-cavity lasers, we are limited by the amount of power that can be deposited into a device before detrimentally affecting the NPLs, possibly due to heating. Hence, we conclude that, at cryogenic temperatures, we are able to achieve larger material gains than at room temperature as we can pump further above the optical-gain threshold of our NPLs before introducing damage. Furthermore, we expect that the losses in the Ag are slightly less at cryogenic temperatures than at room temperature.<sup>S2</sup> The temperature dependence of our metallic-cavity lasers falls in line with the modal gain calculations of our waveguide model.

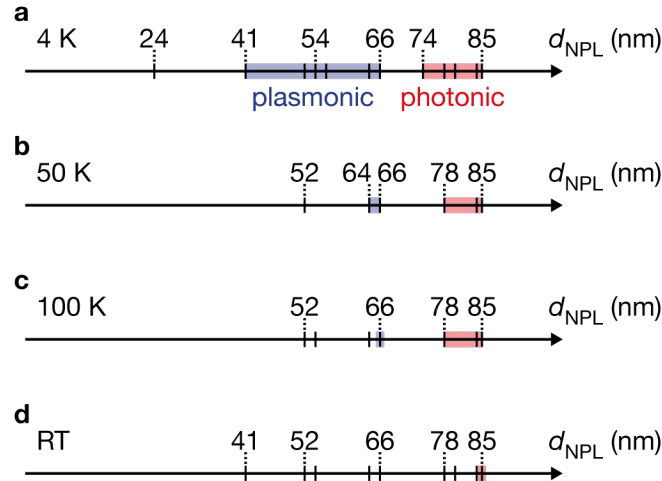


**Figure S1.** Temperature dependence of laser devices. Multiple NPL laser devices were measured at 4 K [(a)], 50 K [(b)], 100 K [(c)], and room temperature [RT; (d)]. Each tick mark on the axis corresponds to a device with given NPL-stripe thickness. The colored shading indicates which type of mode, plasmonic (blue) or photonic (red), lased in each device. Tick marks outside of any colored shading represent devices for which lasing could not be attained.

## Section S2. Major Loss Channels

Besides the Ag and reflection losses, scattering could also lead to losses. However, scattering losses are neglected in the lasing condition (eq 1 in the main text) because it is expected that the Ag and reflection losses play a more significant role. To verify this assumption, we look at the emission intensity of the NPL stripe and compare it to the intensity arising from the reflector edge when the cavity is pumped above threshold (Figure

S2). The reflector edges light up more brightly than the rest of the stripe. The NPL stripes look very uniform in intensity, suggesting that the NPLs form a smooth film and do not provide scattering centers. Furthermore, from our modal-gain calculations, we find that the Ag losses (corresponding to the negative modal gain for  $G_{\text{mat}} = 0 \text{ cm}^{-1}$ ; dotted lines in Figure 3) are much greater than the reflection losses (grey line in Figure 3) for most gain-layer thicknesses. Thus, we conclude that scattering losses can be neglected in the lasing condition, whereas Ag and reflection losses should be taken into consideration.

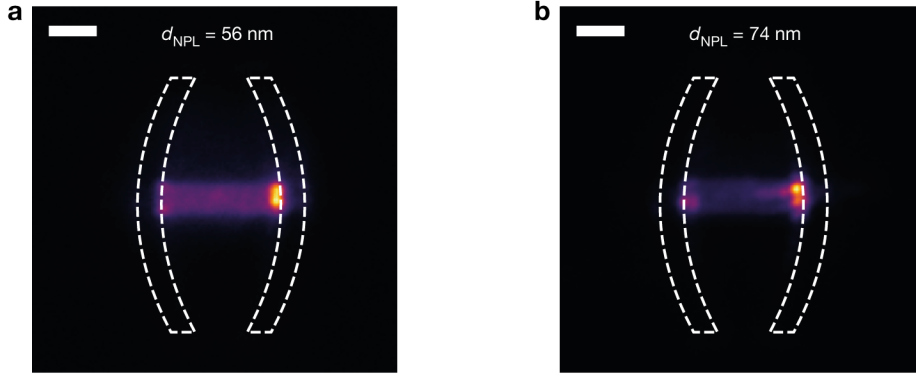


**Figure S2.** Metallic-cavity-laser images above threshold. (a) Image of a device with a 56-nm-thick NPL layer pumped well above the lasing threshold (pump fluence  $37 \mu\text{J}/\text{cm}^2$ ). (b) Image of a device with a 74-nm-thick NPL layer pumped well above the lasing threshold (pump fluence  $23 \mu\text{J}/\text{cm}^2$ ). The devices in (a) and (b) lased in the plasmonic and photonic mode, respectively, and correspond to the devices probed to obtain the spectra in Figure 2a–d and the light–light curves in Figure 4a,b. The white dotted lines show the outline of the cavity reflectors. The colors are scaled to the maximum and minimum of the image. The scale bars are  $4 \mu\text{m}$ .

### Section S3. Lasing Condition

At the lasing threshold, the electric-field amplitude,  $E_0$ , at an arbitrary point in the cavity returns to its original value after one cavity round trip:<sup>S3-5</sup>

$$E_0 = E_0 \sqrt{R_1 R_2} e^{ik_z 2L_{\text{cav}}}. \quad (\text{S1})$$

Here,  $R_1 = R_2 = R$  is the mirror reflectivity,  $k_z$  the propagation constant of the mode, and  $L_{\text{cav}}$  the cavity length.

This requirement can be split into a phase and amplitude condition:

$$m \frac{\lambda_0}{n_{\text{eff}}} = 2L_{\text{cav}}, \quad (\text{S2})$$

$$G_{\text{mod}} \geq -\frac{\ln(R)}{L_{\text{cav}}}, \quad (\text{S3})$$

where  $m$  is an integer number,  $n_{\text{eff}}$  the effective mode index, and  $G_{\text{mod}} = -2k_z''$  the modal gain, which can be expressed in terms of the imaginary part of the propagation constant,  $k_z''$ . The phase condition (eq S2) requires integer multiples of the modal wavelength to fit into a round-trip cavity length, while the amplitude condition (eq S3) dictates the modal gain to be at least as large as the round-trip reflection losses. (Since we are not interested in a steady-state laser oscillation, the modal gain can also be larger than the round-trip reflection

losses.) Note that we ignore scattering losses of the NPL stripe and only consider Ag losses (included in the modal gain) and reflection losses at the reflectors as possible loss channels (see Section S2).

#### Section S4. Estimation of Mirror Reflectivity of Ag Reflectors

The mirror reflectivity can be estimated with the transfer-matrix method<sup>S6,S7</sup> applied to a three-layer stack with the first layer being an effective medium with the complex effective index of the plasmonic and photonic modes, the second layer being a 10-nm-thick alumina film, and the third layer being Ag (Figure S3a). For alumina and Ag, the refractive indices obtained by ellipsometry were used (see Section S13). The reflection and transmission coefficients used for the transfer-matrix method were calculated as described in Ref. S8. The as-obtained mirror reflectivities are high ( $> 97\%$ ) for both the plasmonic and photonic modes (Figure S3b). The actual reflectivities are lower than the calculated values, as scattering at the top of the 500-nm-tall reflectors is ignored.<sup>S9,S10</sup> Therefore, we assume a reflectivity of  $\sim 90\%$  for both modes. For simplicity, we keep the reflectivity constant for all gain-layer thicknesses. As long as the reflectivity is high, the precise value is insignificant because the cavity losses are dominated by propagation losses (i.e., the ohmic losses in the Ag). A thorough discussion on the influence of the reflectivity on the reflection losses and the lasing mode is presented in Section S9.

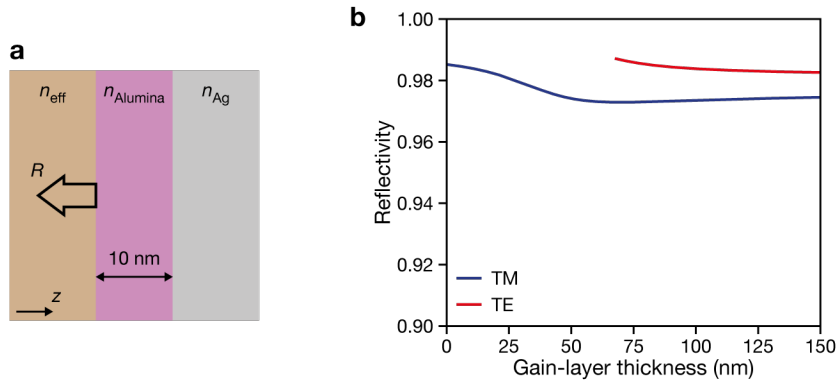


**Figure S3.** Estimation of the mirror reflectivity. (a) Three-layer stack used to calculate the mirror reflectivity,  $R$ , using the transfer-matrix method. The first layer (brown) has the effective index of the TM and TE modes as refractive index, the second layer is a 10-nm-thick alumina film (purple), and the third layer is Ag (grey). The mode propagates in the  $z$ -direction towards the Ag layer. (b) Calculated reflectivity values as a function of gain-layer thickness for the three-layer stack in (a) for the plasmonic (TM, blue) and photonic (TE, red) modes. The true reflectivity values are lower, as scattering at the top of the 500-nm-tall reflectors is ignored in the transfer-matrix method.

#### Section S5. Confinement Factor, Propagation Length, and Threshold Gain

The confinement factor,  $\Gamma$ , is extracted from the linear relationship between the modal gain,  $G_{\text{mod}}$ , and the material gain,  $G_{\text{mat}}$  (see eq 2 in the main text). The slope defines the confinement factor and the  $y$ -axis offset corresponds to the negative inverse of the propagation length,  $L_{\text{prop}}$ , for a transparent gain layer ( $G_{\text{mat}} = 0$ ). We

calculate the modal gain for various material gain values using the multilayer-waveguide model (Figure S4a). Then, we fit eq 2 from the main text to the result to obtain the confinement factor and the propagation length. This procedure is repeated for a range of gain-layer thicknesses (Figure S4b,c). The threshold gain is obtained through eq 4 in the main text (Figure S4d). In principle, an analytical expression for the confinement factor in layered waveguide structures can be used to determine the confinement factor.<sup>S4,S11,S12</sup> However, extracting the confinement factor from a linear fit to the modal gain can also be employed for more complex structures (i.e., structures that are not invariant in the propagation direction) for which no analytical expression exists.

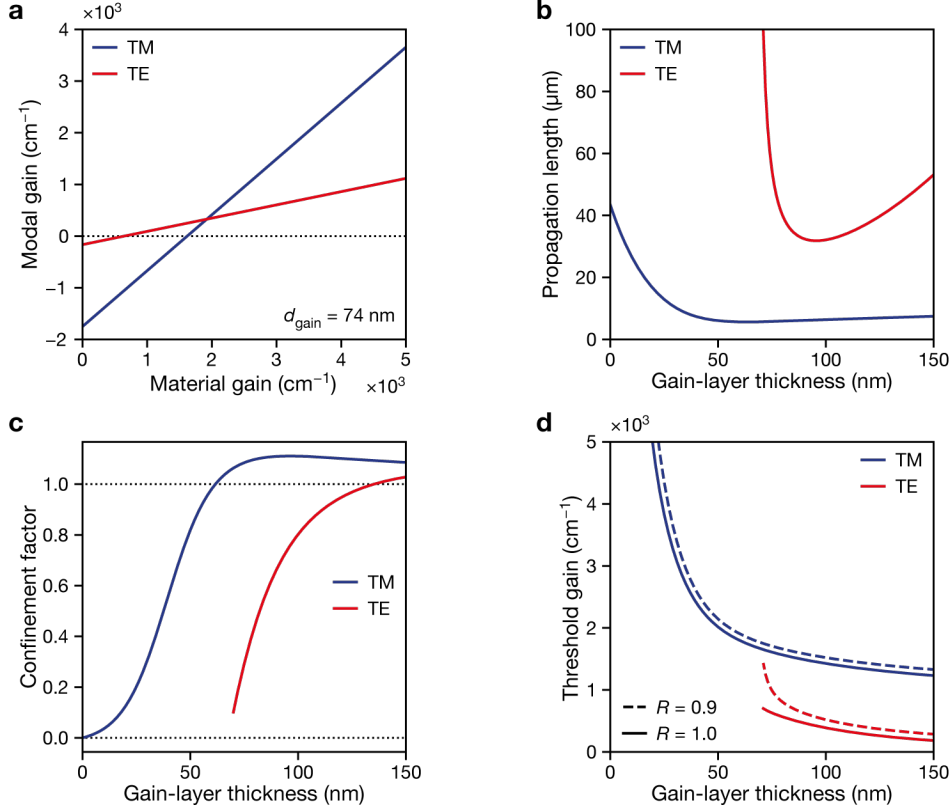


**Figure S4.** Calculated confinement factor and threshold gain. (a) Modal gain as a function of material gain calculated for a waveguide structure with  $d_{\text{gain}} = 74 \text{ nm}$ . The linear relationship is used to extract the confinement factor and the propagation length for the plasmonic (TM, blue) and photonic (TE, red) modes. (b) Propagation length as a function of gain-layer thickness. (c) Confinement factor as a function of gain-layer thickness. (d) Threshold gain as a function of gain-layer thickness. Here, the threshold gain was calculated without reflection losses ( $R = 1.0$ ) and for a reflectivity  $R = 0.9$ .

## Section S6. Gap-Layer Design Criteria

As discussed in the main text, we find that for a HIG layer, the threshold gain for plasmonic lasing in devices with thin gain-layers is reduced compared to a LIG layer. Those conclusions were made for a multilayer-waveguide structure consisting of Ag at the bottom, a 10-nm-thick gap layer with a high or low refractive index, a NPL gain layer, and air on top. For the gain layer, the NPL refractive index at a vacuum wavelength  $\lambda_0 = 635 \text{ nm}$  is  $n_{\text{NPL}} = 1.89$  (see Section S13). The refractive index of bulk semiconductor materials, which are commonly used as gain media for nanolasers, is usually much larger. Therefore, we

calculate the modal gain for a waveguide structure that employs a gain layer with a refractive index of  $n_{\text{CdS}} = 2.5$  (representing bulk cadmium sulfide) at a free-space wavelength of  $\lambda_0 = 635$  nm (Figure S5a) and a structure with  $n_{\text{InGaAs}} = 3.5$  (representing bulk indium gallium arsenide) at a free-space wavelength of  $\lambda_0 = 1550$  nm (Figure S5b). For the case of  $n_{\text{CdS}} = 2.5$  and  $\lambda_0 = 635$  nm, the plasmonic-mode threshold gain for gain-layer thicknesses slightly below the photonic-mode cutoff thickness is reduced for the HIG structure, even if reflection losses are neglected ( $R = 1.0$ ). For the case of  $n_{\text{InGaAs}} = 3.5$  and  $\lambda_0 = 1550$  nm, even for gain-layer thicknesses far above the photonic-mode cutoff thickness, the threshold gain is lower for the HIG structure.

Furthermore, we compare our hypothetical LIG and HIG structures (with the NPL refractive index for the gain layer and  $\lambda_0 = 635$  nm) to the experimentally studied waveguide structure with an alumina gap layer ( $n_{\text{gap}} = 1.64$ ) and to a structure without a gap layer (Figure S5c). Avoiding a gap layer increases the overlap of the plasmonic mode (and also to a small extent the overlap of the photonic mode) with the gain layer, which reduces the threshold gain. For gain layers with  $d_{\text{gain}} < 41$  nm, the threshold gain for the structure without gap layer (blue dotted line in Figure S5c) starts to increase more steeply than for the other structures. This is a consequence of the overall waveguide structure being 10 nm thinner without the gap layer. The reduction in the overall thickness becomes also apparent for the photonic mode for which the cutoff thickness is shifted by 10 nm toward thicker gain layers. Even though removing the gap layer could potentially enable plasmonic lasing for very thin devices, it likely also compromises device lifetime, as exposure to ambient conditions can detrimentally affect the Ag quality.

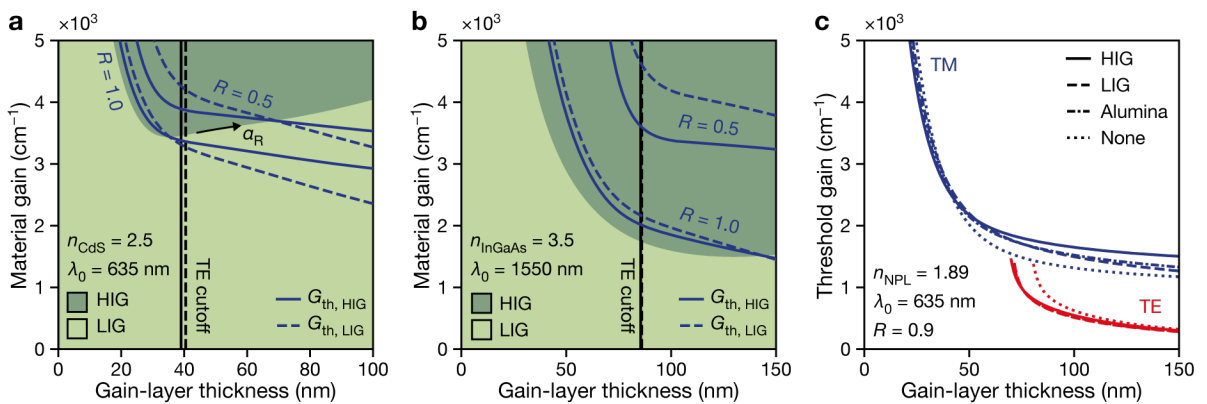


**Figure S5.** Threshold gain for various gain and gap layers. (a, b) Material gain at which the modal gain is larger for the HIG (dark-green area) or LIG (light-green area) layer for a structure with a gain-layer refractive index of  $n_{\text{CdS}} = 2.5$  and a free-space wavelength  $\lambda_0 = 635$  nm [(a)], and  $n_{\text{InGaAs}} = 3.5$  at  $\lambda_0 = 1550$  nm [(b)]. The threshold gains,  $G_{\text{th}}$ , for the plasmonic modes of the HIG and LIG structures are plotted as solid and dashed blue lines, respectively. They are calculated for a 10- $\mu\text{m}$ -long cavity without reflection losses ( $R = 1.0$ ) and for a mirror reflectivity  $R = 0.5$ . For increasing reflection losses,  $\alpha_R$ , the threshold-gain crossing point moves along the mode-condition border in the direction of the arrow [only shown in (a)]. The black vertical solid and dashed lines indicate the photonic-mode (TE) cutoff thickness for the HIG and LIG structures, respectively. (c) Threshold gain for plasmonic modes (TM, blue) and photonic modes (TE, red) calculated for a NPL gain layer ( $n_{\text{NPL}} = 1.89$ ) and various gap layers at  $\lambda_0 = 635$  nm. The cavity length is 10  $\mu\text{m}$  and the mirror reflectivity  $R = 0.9$ .

## Section S7. Inflection Strength of Light–Light Curve at Threshold

We can simplify the relationship between the pump power and the output-photon number to a regime above and below threshold. Therefore, we need to look through which channels the excited carrier population decays and to what fractions (see eq S5 and S6 in Section S15). Below threshold, the stimulated-emission term accounts for reabsorption (the material gain is negative) and thus does not contribute to a loss of carriers. Therefore, non-radiative decay and spontaneous emission are the only carrier-decay channels, summing to a total decay rate of  $1/(\tau_{\text{sp}}\Phi)$ , where  $\tau_{\text{sp}}$  is the spontaneous-emission lifetime and  $\Phi$  the quantum yield of the gain medium. The rate of carriers that feed into the surface plasmon or photon populations is described solely by the spontaneous-emission term  $\beta_i/(\tau_{\text{sp}})$  with the spontaneous-emission factor  $\beta_i$  of the mode  $i$  ( $i = \text{TM}, \text{TE}$ ). Thus, the fraction of carriers that decay into a given mode population becomes  $\beta_i\Phi$  below threshold. In contrast, above threshold, stimulated emission dominates and becomes the main decay channel for carriers. Therefore, we can assume that nearly all excited carriers decay into the lasing mode, resulting in a carrier-to-mode fraction of unity. Consequently, the difference in output-photon number below and above threshold (we can assume the output-photon number is proportional to the carrier-to-mode fraction) is on the order of  $1 - \beta_i\Phi$ , giving rise to a strong inflection in the light–light curve at the lasing threshold if  $\beta_i\Phi$  is considerably smaller than unity.

## Section S8. Spontaneous-Emission-Factor Calculation

We estimate the fraction of spontaneous emission into a specific target mode,  $\beta_i$ , using the formalism described in Ref. S13, providing exact solutions to Maxwell’s equations for the power dissipated by an electric-dipole source in a multilayer structure. In brief, we treat the NPLs as randomly oriented electric-dipole sources in the gain layer of our multilayer-waveguide structure and calculate the position-averaged fraction of power dissipated into the target mode. The multilayer structure was modeled as a semi-infinite layer of Ag at the bottom, 10 nm of alumina, a gain layer of thickness  $d_{\text{gain}}$ , and a semi-infinite air layer on top, resulting in the same structure as used for waveguide-mode calculations described in the main text. The permittivities of Ag, alumina, and the gain layer (NPL layer) were extracted from ellipsometry data at a free-space wavelength  $\lambda_0 = 635$  nm (see Section S13). Only the real part of the permittivity of the NPL film was retained in our approximation of  $\beta_i$  to model spontaneous emission at excitation fluences just below the transparency of the gain medium. For a given gain-layer thickness,  $d_{\text{gain}}$ , we calculated the dissipated power as a function of the in-plane wavevector,  $k_{\parallel}$ , by an electric-dipole source at a height  $x_0$  within the NPL layer (Figure S6a). We considered the random orientation of the NPLs by averaging the power spectra obtained for dipole sources

pointing along the two in-plane directions and the out-of-plane direction at a given height  $x_0$ . Spontaneous emission into the plasmonic and photonic modes are visible as peaks in the as-obtained  $k_{\parallel}$ -resolved dissipated-power spectra (Figure S6b). Each peak is centered around the in-plane wavevector of the corresponding mode. As expected, the peak of the photonic mode is only visible for gain-layer thicknesses above the photonic-mode (TE) cutoff thickness (not shown). The fraction of spontaneous emission into mode  $i$  ( $i = \text{TM}, \text{TE}$ ) for a randomly oriented dipole source at height  $x_0$  within the gain layer was then extracted by integrating the dissipated-power spectrum over the peak corresponding to mode  $i$  and dividing by the total dissipated power by emission into all modes, including emission of free-space photons and quenching in the Ag (integration of the dissipated power spectrum over all  $k_{\parallel}$  from zero to infinity). Finally,  $\beta_i$  was obtained for a given gain-layer thickness by varying  $x_0$  from zero to  $d_{\text{gain}}$  in steps of 2 nm and averaging over the obtained fractions.

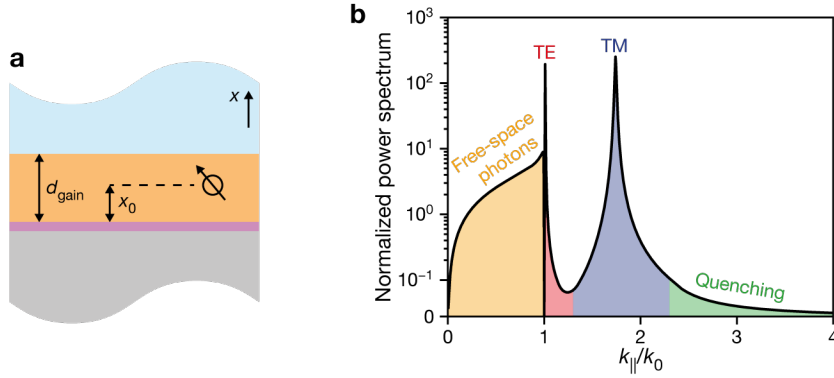


**Figure S6.** Calculation of the spontaneous-emission factor. (a) Schematic of a dipole at height  $x_0 = 40$  nm in a multilayer-waveguide structure with a NPL gain layer of thickness  $d_{\text{gain}} = 74$  nm. (b) Dissipated-power spectrum as a function of the in-plane wavevector,  $k_{\parallel}$ , normalized by the free-space wavevector,  $k_0 = 2\pi/\lambda_0$ , for the geometry in (a). The spectrum is averaged over two in-plane directions and the out-of-plane direction of a dipole. The shaded areas indicate the range of integration for various modes: free-space photons (orange), photonic mode (TE, red), plasmonic mode (TM, blue), and quenched emission (green).

## Section S9. Effect of Mirror Reflectivity on Lasing Mode

For the results in the main text, we have assumed equal mirror reflectivity for plasmonic and photonic modes. Here, we would like to explore how the reflection losses influence the threshold gain and how separate tuning of the modal reflectivities can potentially suppress the photonic mode in devices with gain-layer thicknesses above the photonic-mode (TE) cutoff thickness.

The reflection losses can be calculated using eq S3 (the losses are equal to the expression on the right-hand side). Both the cavity length and mirror reflectivity will influence the reflection losses when expressed as round-trip loss. For smaller cavities and lower mirror reflectivity, the reflection losses increase (Figure S7a). The influence of reflection losses on the threshold gain is inversely proportional to the confinement factor (see eq 4 in the main text). Hence, the threshold gain for the photonic mode strongly increases as its cutoff gain-



layer thickness is approached (Figure S7b). This now gives two possible tuning knobs for enabling plasmonic lasing in devices that support both plasmonic and photonic modes: selectively decreasing the reflectivity of the photonic mode or decreasing the reflectivity of both modes in a device operating slightly above the photonic-mode cutoff thickness.

Figure S7c outlines, for a given gain-layer thickness, which mode experiences a lower threshold gain. Any combination of mode reflectivities below (above) a given gain-layer-thickness line will result in a lower threshold gain for the plasmonic (photonic) mode. For thick gain layers ( $d_{\text{gain}} = 150$  nm, black line in Figure S7c), a low but equal reflectivity is not sufficient to lift the photonic threshold gain above the plasmonic threshold gain. In this case, the photonic-mode reflectivity must be substantially decreased compared to the plasmonic-mode reflectivity to achieve a lower threshold gain for the plasmonic mode.

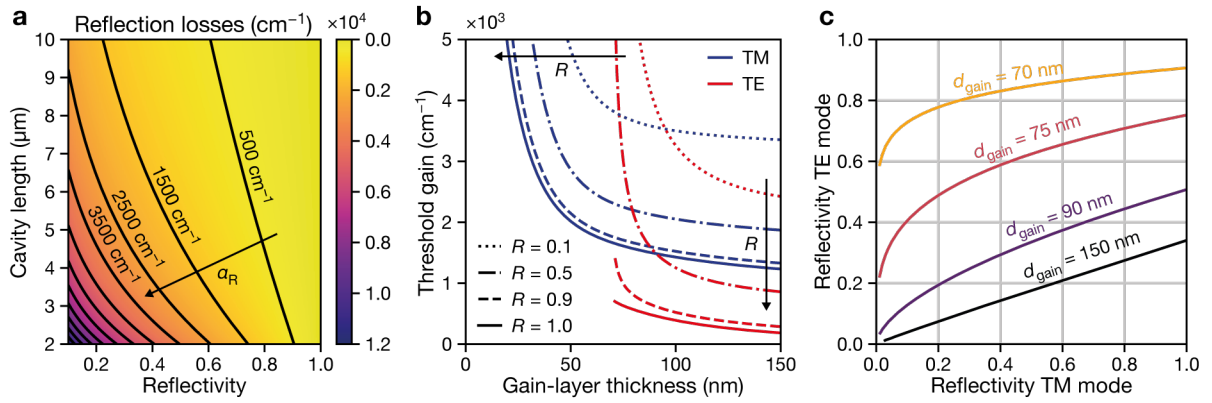


**Figure S7.** Influence of mirror reflectivity on lasing mode. (a) Reflection losses,  $\alpha_R$ , arising from partially reflective mirrors are plotted as a function of mirror reflectivity and cavity length. The arrow points in the direction of increasing reflection losses. (b) Threshold gain for plasmonic (TM, blue lines) and photonic (TE, red lines) modes as a function of gain-layer thickness for a 10- $\mu\text{m}$ -long cavity and various reflectivity values,  $R$ . Arrows indicate increasing mirror reflectivity. (c) Plasmonic (TM) and photonic (TE) mode reflectivity map. For a given gain-layer thickness (indicated by the line label), each point on the line indicates a combination of plasmonic and photonic mode reflectivities that results in the same threshold gain for both modes. A combination of plasmonic and photonic mode reflectivities below (above) a given gain-layer-thickness, results in a lower threshold gain for the plasmonic (photonic) mode. A cavity length of 10  $\mu\text{m}$  was used for this calculation.

## Section S10. Fabrication of Laser Cavities

The Ag cavities were fabricated by template stripping to achieve a smooth Ag surface.<sup>S14</sup> The template was prepared from a 1-mm-thick, 2-inch-diameter, <100> silicon wafer. The wafer was prepared with a 280-nm-thick positive electron-beam resist (Allresist, CSAR AR-P 6200.09). After electron-beam exposure (Vistec Lithography, EBP 5200+), the resist was developed (Allresist, AR 600-546) for 1 min, revealing a negative mask of the cavity reflectors on top of the silicon wafer. The cavity length was 10  $\mu\text{m}$ , the curved reflector is a parabola with a radius of curvature of 20  $\mu\text{m}$ , the reflector width was 2  $\mu\text{m}$ , and the reflector length was 21.2  $\mu\text{m}$ . The curved shape of the reflectors leads to a stable Fabry–Pérot resonator.<sup>S3</sup> The wafer was etched ~500 nm deep using a hydrogen-bromide-based inductively-coupled-plasma reactive-ion etch (Oxford

Instruments, Plasmalab System 100, 80 W radio-frequency power, 800 W inductively-coupled-plasma power, 50°C) for 150 s. The resist was removed by applying oxygen plasma (PVA TePla, GIGAbatch 310M) at 600 W for 5 min and subsequently dipping the silicon template into buffered hydrofluoric acid (Technic France, 1:7 hydrofluoric acid in ammonium fluoride) for 10 s. Finally, the template was cleaned in a Piranha solution [1:1 sulfuric acid (Sigma-Aldrich, 95.0–97.0%) and hydrogen peroxide (VWR Chemicals, 30%)] for 15 min.

Before Ag was deposited onto the template, it was cleaned in nitric acid (Sigma-Aldrich,  $\geq 65\%$ ) for 15 min and rinsed with ultrapure water (18 M $\Omega$  cm) for  $\sim 3$  min. Then, the template was sonicated in ultrapure water and isopropanol (Sigma-Aldrich,  $\geq 99.5\%$ ) for 10 min each. A thermal evaporator (Kurt J. Lesker, Nano36) was used to deposit a  $\sim 700$ -nm-thick film of Ag (Kurt J. Lesker, 99.99%). The deposition was performed at a base pressure of  $< 9 \times 10^{-8}$  mbar and at a deposition rate of 25 Å/s while the template was rotated at 60 rpm. A microscope slide was bonded to the Ag film using epoxy (Epoxy Technology, EPO-TEK OG116-31) cured under ultraviolet light for 2 h.

The Ag cavities were stripped manually from the template shortly before they were loaded into an atomic-layer deposition chamber (Picosun, Sunale R-150). A 10-nm-thick alumina layer was deposited at 50 °C applying 100 atomic-layer deposition cycles. Each cycle consisted of a 0.2 s trimethylaluminum pulse (Sigma Aldrich Fine Chemicals, electronic grade) at a flow rate of 200 sccm, a 10 s nitrogen purge, a 0.5 s water pulse (ultrapure, 18 M $\Omega$  cm) at a flow rate of 200 sccm, and a 30 s nitrogen purge.

For depositing the gain medium, CdSe/Cd<sub>x</sub>Zn<sub>1-x</sub>S core/shell NPLs having a 4-monolayer-thick CdSe core and a 2-nm-thick shell were synthesized according to Ref. S15. The ink for the electrohydrodynamic nanoprinting was prepared by transferring the NPLs from hexane to tetradecane through selective evaporation while adjusting the concentration to an optical density of 5.0 (measured at the lowest-energy exciton peak using a quartz cuvette with a 10-mm path length). A description of the nanoprinting setup can be found elsewhere.<sup>S16</sup> 0.5  $\mu$ L of the NPL ink was injected into the metal-coated nozzle with an outer diameter of  $\sim 1.7$   $\mu$ m. To eject ink, 250 V direct current were applied between the nozzle (+) and the indium-tin-oxide-coated-glass sample holder (ground). The distance between the nozzle and the metallic-cavity sample was kept at 5–10  $\mu$ m. The stripes of 10  $\mu$ m length and 2  $\mu$ m width were generated by moving the sample stage in a serpentine-like fashion to print nine parallel lines at a pitch of 250 nm. Different stripe thicknesses were produced by varying the number of overprints.

To determine the required stage velocity and number of overprints for a given stripe thickness, a parameter sweep was performed using the same ink-loaded nozzle. Specifically, stripes were printed on a flat Ag–alumina

substrate (which was fabricated in the same batch as the Ag-cavity sample) applying stage velocities from 4 to 16  $\mu\text{m/s}$ , while the number of overprints was increased from one to ten. A dark-field reflection image (taken with a Nikon CFI LU Plan Fluor BD 50 $\times$  objective with a numerical aperture of 0.8 on a Nikon Eclipse LV100 microscope) of the printed stripes was used to estimate the obtained stripe thickness for a given parameter combination by comparing the color of the stripe (the stripe waveguide can only accept certain input wavelengths) to a reference image of stripes whose thicknesses were determined by atomic force microscopy. Afterwards, stripes were printed into multiple cavities using the predefined stage velocities and overprint numbers to yield stripes with thicknesses between 20 and 90 nm. After all optical measurements were performed, the stripe thickness of each device was measured using atomic force microscopy (Bruker, Dimension FastScan). Scanning-electron micrographs of laser devices were acquired on a scanning-electron microscope (Hitachi, S-4800).

## Section S11. Optical Characterization

All optical measurements were performed in a closed-cycle helium cryostat (Montana Instruments, Cryostation 2 with LWD option) under vacuum and cooled to 4 K. The sample was mounted on a piezo-positioning system (Attocube, 1 $\times$ ANPz101 and 2 $\times$ ANPx101) inside the cryostat.

To obtain cavity spectra within the spontaneous-emission bandwidth of the NPLs, light from a 385-nm LED (Thorlabs, M385LP1) was used for wide-field excitation. The light from the LED was passed through a 400-nm/40-nm-bandwidth bandpass filter (Thorlabs, FBH400-40), deflected at a 400-nm dichroic longpass filter (Omega Optical, 400DCLP), again deflected at a 405-nm dichroic longpass filter (AHF analysentechnik, F48-403), and imaged through the cryostat window onto the sample plane using a 60 $\times$  extra-long-working-distance objective (Nikon, CFI S Plan Fluor ELWD with a numerical aperture of 0.7).

Lasing experiments were performed with a 405-nm pulsed laser source ( $\sim$ 340 fs pulse duration, 1 kHz repetition rate) as excitation. The laser pulses emerged from a collinear optical parametric amplifier (Spectra-Physics, Spirit-OPA) pumped by a 1040-nm laser (Spectra-Physics, Spirit-1040-8). After spectral filtering, the beam was passed through a reflective, graduated neutral-density filter wheel to adjust the pulse power. Then, it was directed through a beam-expanding telescope and a half-wave plate (Thorlabs, AHWP05M-600). The beam passed through a 500-nm (Thorlabs, FESH0500) and a 750-nm shortpass filter (Thorlabs, FESH0750). Then, a fraction of the beam was deflected onto a photodiode (Thorlabs, S120VC) to monitor the pump power with a power meter (Thorlabs, PM100D). The rest of the beam was passed through a defocusing lens

[achromatic doublet with focal length of 300 mm, (Thorlabs, AC254-300-A-ML)] and the 400-nm dichroic longpass filter (Omega Optical, 400DCLP), and then deflected at the 405-nm dichroic longpass filter (AHF analysentechnik, F48-403). Finally, the beam arrived at the 60× extra-long-working-distance objective from where it passed through the cryostat window and arrived at the sample plane as a defocused spot of  $\sim 30\ \mu\text{m}$  diameter. Since the spectrometer slit appears in the image center, the excitation spot was aligned slightly off-center to conform with the center of the NPL stripe of the probed cavity.

The same 60× extra-long-working-distance objective was used for emission collection. The emission was directed through the 405-nm dichroic longpass filter (AHF analysentechnik, F48-403), a 450-nm longpass filter (Thorlabs, FEL0450) and relayed by six 200-mm focal-length achromatic doublets (Thorlabs, five AC254-200-A-ML and one AC508-200-A-ML) into an imaging spectrometer (Andor, Shamrock 303i) with the entrance slit set to  $50\ \mu\text{m}$ . Inside the spectrometer, the emission was horizontally dispersed by a 300 lines/mm grating (500-nm blaze) and imaged with an air-cooled electron-multiplying charged-coupled-device camera (Andor, iXon 888 Ultra). The sample was positioned such that the vertical entrance slit of the imaging spectrometer aligned onto the inner edge of one of the reflectors of the probed cavity. Each spectrum presented in the main text displays a single pixel row on the camera taken at the maximum intensity along the printed NPL stripe width (which roughly coincides with the vertical center of the stripe). One pixel row corresponds to a distance of  $\sim 0.22\ \mu\text{m}$  along the reflector. For the integrated spectra in Figure 5a and b, a single pixel row was integrated for each pump fluence. Integrating over multiple pixel rows did not significantly change the slopes (on the log–log scale) below and above the threshold. For real-space imaging, the zero-order mode of the grating was used in combination with a wide-open slit. For polarization resolved spectra, a linear polarizer (Thorlabs, LPVISB100-MP2) was placed in an image-plane after the 450-nm longpass filter.

To determine the laser-spot diameter, the laser spot was imaged on a dried film of NPLs on the sample. Two perpendicular Gaussians were fitted through the beam center. The average of the distance between the 1/e-values of the Gaussians was taken as the beam diameter.

The pump power at the sample plane was measured using a photodiode (Thorlabs, S170C) in combination with a power meter (Thorlabs, PM100D). This allowed us to determine the conversion factor between the power reading of the photodiode that measured a fraction of the beam during the lasing experiments and the power arriving at the sample.

## Section S12. Multilayer-Waveguide Model

The multilayer-waveguide model was implemented following a theoretical model described in Ref. S17. In short, a general solution to the wave equation is taken, and the boundary conditions derived from Maxwell's equations are imposed at each layer boundary. In the top and bottom semi-infinite slabs, the wave is forced to exponentially decay, so only guided modes are accepted (no leaky modes).<sup>S17,S18</sup> The resulting eigenvalue equation is solved by a minimization algorithm. We solve the eigenvalue equation for TM and TE modes. Within the considered range of gain-layer thicknesses (0–150 nm), only the fundamental TM and TE modes exist.

From the resulting propagation constant,  $k_z$ , we can derive the effective mode index,  $n_{\text{eff}}$ , the modal gain,  $G_{\text{mod}}$ , and the electric- and magnetic-field profiles. The time-averaged electromagnetic energy density,  $\langle u_{\text{EM}} \rangle$ , is calculated as defined by Ref. S19:

$$\langle u_{\text{EM}} \rangle = \frac{1}{4} \varepsilon_0 \left( \varepsilon(\lambda) - \lambda \frac{\partial \varepsilon(\lambda)}{\partial \lambda} \right) |E|^2 + \frac{1}{4} \mu_0 |H|^2 \quad (\text{S4})$$

Here,  $E$  and  $H$  are the electric and magnetic fields, respectively,  $\varepsilon$  and  $\varepsilon_0$  are the relative and vacuum permittivities, respectively,  $\mu_0$  is the vacuum permeability (all materials are assumed to be non-magnetic), and  $\lambda$  denotes the wavelength. To get the total energy,  $U_{\text{EM}}$ , the electric- and magnetic-field intensities are integrated along the out-of-plane direction ( $x$ -direction) from minus to plus infinity. The time-averaged electric-energy density,  $\langle u_{\text{E}} \rangle$ , is calculated using only the electric-field term in eq S4.

As inputs to the model, the free-space wavelength, the permittivity of each constituent material, and the layer thicknesses needed to be defined. For the mode-profile and the modal-gain calculation the free-space wavelength,  $\lambda_0$ , was kept at  $\lambda_0 = 635$  nm (1.95 eV). For the FSR calculations,  $\lambda_0$  was varied over a range of 500–700 nm (1.48–1.77 eV). The relative permittivities were obtained from ellipsometry (see SI Section S13). The alumina layer was considered as lossless [ $\text{Im}(\varepsilon_{\text{gap}}) = 0$ ], while the Ag losses were included as a positive imaginary part of the relative permittivity [ $\text{Im}(\varepsilon_{\text{Ag}}) > 0$ ]. The gain layer was kept lossless for the calculation of the mode profiles and the mode index [ $\text{Im}(\varepsilon_{\text{gain}}) = 0$ ], lossy (as obtained from ellipsometry of a NPL film) for the FSR calculation, and with a positive material gain for the modal-gain calculations [ $\text{Im}(\varepsilon_{\text{gain}}) < 0$ ].

## Section S13. Ellipsometry of NPL, Ag, and Alumina Films

To obtain the relative permittivity of the gain layer for the multilayer-waveguide calculations, ellipsometry was performed on a film of NPLs. NPLs dispersed in hexane with an optical density of 2.0 (measured at the lowest energy exciton peak using a quartz cuvette with a 10-mm path length) were mixed

with octane (Sigma-Aldrich, 98%) in an 8:1 volumetric ratio. Then, 35  $\mu\text{L}$  of the mixture was dropcast on a 20 mm  $\times$  20 mm, <100> silicon chip. A reference silicon chip of the same wafer was kept for determining the thickness of the native-oxide layer. Ellipsometry was performed on a J.A. Woollam VASE ellipsometer. Measurements were collected at four angles (60°, 65°, 70°, and 75°) in the wavelength range 300–1000 nm in steps of 1 nm in reflection mode. A Kramers–Kronig-consistent dispersion model was fitted to the obtained data. The film thickness was fitted together with a Tauc–Lorentz oscillator in the transparent spectral region of 700–1000 nm. Then, the spectral region was successively increased towards the blue wavelength regime, while in total five Gaussian oscillators were added to conform with the excitonic features at the band edge. The mean squared error of the final fit was 2.2. The fitted NPL-film thickness was confirmed with a cross-sectional scanning-electron-microscope image. From the dispersion model, the complex refractive index was extracted (Figure S8a), and the relative permittivity was then derived from these data. To mimic the blue shift of the NPL bandgap when cooled to cryogenic temperatures, the refractive index values were shifted by 18 nm to the blue, corresponding to the shift in the photoluminescence spectrum. The complex relative permittivity,  $\epsilon_{\text{gain}}$ , was then obtained through  $\epsilon_{\text{gain}} = (n + ik)^2$ , with  $n$  and  $k$  being the real and imaginary part of the complex refractive index and  $i$  being the imaginary unit. (Note that for the modal gain calculations, the real part of the relative permittivity was set to  $\epsilon'_{\text{gain}} = n^2$ , while the imaginary part was swept over a range of values obtained from eq 7 in the main text.)

To determine the relative permittivity of Ag, a Ag film was template-stripped from a flat region of a silicon template immediately before an ellipsometry scan in reflection mode was performed (angles 65°, 70°, 75°; scan range 400–1700 nm in steps of 10 nm). The optical constants were obtained by a numerical fit to the experimental data (Figure S8b), and the complex relative permittivity,  $\epsilon_{\text{Ag}}$ , was derived by employing  $\epsilon_{\text{Ag}} = (n + ik)^2$ .

For acquiring the permittivity values of alumina, an alumina film was prepared by atomic-layer deposition onto a <100> silicon chip, using the same deposition parameters as for the device fabrication (see Section S10). A reference silicon chip of the same wafer was used to determine the thickness of the native-oxide layer. An ellipsometry scan in reflection mode was performed shortly after the deposition (angles 65°, 70°, 75°; scan range 400–900 nm in steps of 10 nm). Then, a transparent Cauchy model was fitted to the experimental data, the refractive index was extracted (Figure S8c), and the relative permittivity was calculated using  $\epsilon_{\text{gap}} = n^2$ .

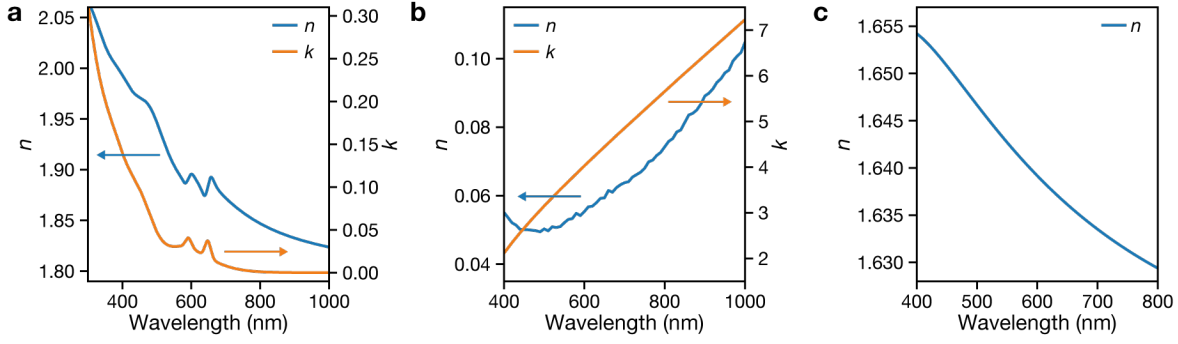


**Figure S8.** Complex refractive index of NPL, Ag, and alumina films. (a) Complex refractive index ( $\tilde{n} = n + ik$ ) of a dropcast NPL film obtained with ellipsometry in reflection mode. A Kramers-Kronig-consistent dispersion model comprising a Tauc-Lorentz and five Gaussian oscillators were fitted to the ellipsometry data. The mean squared error of the fit was 2.2. The data displayed here do not include the 18-nm blue shift to imitate the bandgap shift at cryogenic temperatures. (b) The Ag refractive index was obtained with ellipsometry performed on a flat, template-stripped Ag film. Through numerical fitting of the experimental data, the complex refractive index was obtained. (c) An alumina film was prepared in the same manner as for the device fabrication but on a silicon substrate. Ellipsometry data was acquired and a transparent Cauchy model was fitted to extract the refractive index.

## Section S14. Waveguide Dispersion

The dispersion of the effective index was calculated by sweeping over the free-space wavelength in the multilayer-waveguide model. The waveguide formed by the gain layer strongly influences the effective mode index (Figure S9a). The mode index is highly dispersive (Figure S9b), not only because the constituent materials are dispersive, but also because the gain layer forms a waveguide that introduces waveguide dispersion. As a consequence, the group index takes large values (Figure S9c).

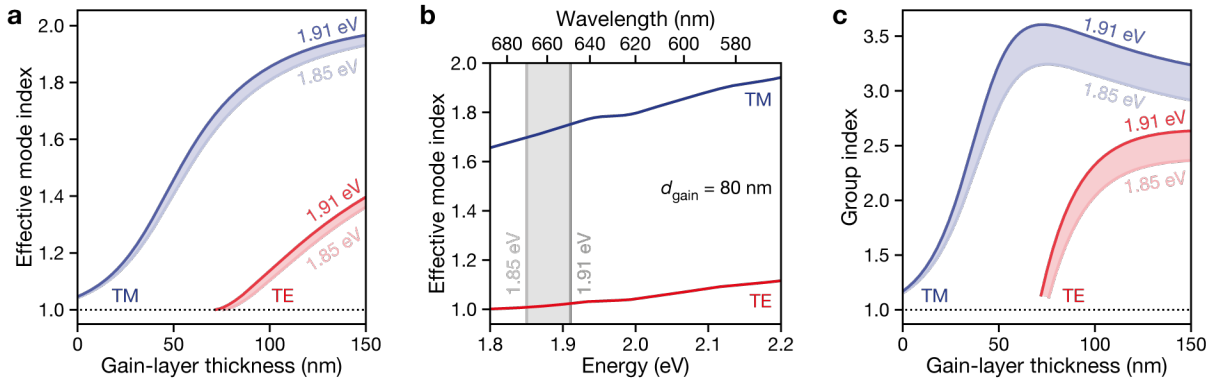


**Figure S9.** Effective index dispersion. (a) Effective mode index in the range 1.85–1.91 eV (lines and shaded areas) for the plasmonic (TM, blue) and photonic (TE, red) mode. (b) Dispersion of the effective mode index for a gain-layer thickness of 80 nm for the plasmonic (TM, blue) and photonic (TE, red) mode. The grey shaded region indicates the range 1.85–1.91 eV. (c) Group index in the range 1.85–1.91 eV (lines and shaded areas) for the plasmonic (TM, blue) and photonic (TE, red) mode as a function of gain-layer thickness.

## Section S15. Laser Rate Equations

The coupled-rate-equation model was set up following Refs. S6 and S20:

$$\frac{dN}{dt} = \frac{\eta_P P(t)}{E_P} - \frac{N}{\tau_{sp}} - k_1 N - \sum_i v_{g,i} \Gamma_i G_{\text{mat}}(N) S_i, \quad (\text{S5})$$

$$\frac{dS_i}{dt} = v_{g,i} \left( \Gamma_i G_{\text{mat}}(N) - \frac{1}{L_{\text{prop},i}} + \frac{\ln(R)}{L_{\text{cav}}} \right) S_i + \beta_i \frac{N}{\tau_{\text{sp}}}, \quad (\text{S6})$$

with  $t$  being the time,  $N$  the excited-carrier population,  $S_i$  the surface-plasmon and photon populations, respectively, with  $i$  indicating the mode ( $i = \text{TM}, \text{TE}$ ). For laser cavities with gain-layer thickness above the photonic-mode-cutoff thickness, a surface-plasmon,  $S_{\text{TM}}$ , and a photon,  $S_{\text{TE}}$ , mode population were considered, while for laser cavities with gain-layer thicknesses below the photonic-mode cutoff thickness, only a surface-plasmon mode population,  $S_{\text{TM}}$ , was taken into account.  $\eta_p$  is the fraction of pump power absorbed by the gain layer (it is estimated using the transfer matrix method; see Section S16),  $E_p$  the energy of the pump photon (at 405 nm), and  $P(t)$  the optical pump power. The time dependence of the optical pump power is modeled as a squared hyperbolic secant function:<sup>S21</sup>  $P(t) = P_p \text{sech}^2(1.76t/\Delta t)$ , with the peak power  $P_p = 0.88 E_{\text{pulse}}/\Delta t$ , the energy of the pump pulse  $E_{\text{pulse}}$ , and the pulse duration  $\Delta t = 340$  fs.  $\tau_{\text{sp}}$  and  $k_1$  are the spontaneous-emission lifetime and the non-radiative recombination rate, respectively. Both are estimated from the total lifetime  $\tau_{\text{tot}} = 5$  ns and the quantum yield of our NPLs in solution,  $\Phi = 0.88$  (Ref. S15), as  $\tau_{\text{sp}} = \tau_{\text{tot}}/\Phi$  and  $k_1 = 1/\tau_{\text{tot}} - 1/\tau_{\text{sp}}$ . Note, that we do not include any Auger-recombination term in the rate equations, as evidence suggests that Auger processes in NPLs are suppressed at cryogenic temperatures.<sup>S22</sup> The group velocity of mode  $i$  is defined through  $v_{g,i} = c/n_{g,i}$ , where  $n_{g,i}$  is the group index of mode  $i$  (defined in eq 6 in the main text). The confinement factor  $\Gamma_i$  and the propagation length  $L_{\text{prop},i}$  were obtained from the modal-gain calculations (see Section S5). The material gain  $G_{\text{mat}}(N)$  for the NPL layer was modeled with a logarithmic function with parameters fitted from data in Ref. S23 (see Section S17). The mirror reflectivity  $R = 0.9$  and the cavity length  $L_{\text{cav}} = 10 \mu\text{m}$  were kept the same for the plasmonic and photonic modes.  $\beta_i$  denotes the spontaneous-emission factor and was estimated by calculating the branching ratio of an orientation- and position-averaged electric dipole in the multilayer-waveguide structure (see Section S8).

The mirror loss rate, defined as  $v_{g,i} \ln(R)/L_{\text{cav}} S_i$ , was integrated over time to obtain the output-photon number. Here, it is assumed that all surface plasmons and photons lost through imperfect mirror reflection contribute to the output-photon number. In our experiments, only a portion of the surface plasmons and photons scatter to photons within the collection cone of our objective. We assume a linear relation between the portion of collected light and electromagnetic intensity inside the cavity modes. This allows us to compare the output-photon number to integrated-intensity values from experiments.

Further, we ignore modal cross-coupling and the Purcell enhancement in our rate-equation model. As the field components of the plasmonic and photonic mode are orthogonal to each other, no direct cross-coupling



is expected. Thus, no cross-coupling terms between the surface-plasmon and photon populations are included. The surface-plasmon and photon populations indirectly interact with each other through the carrier population. The Purcell enhancement is neglected in the rate-equation model, as it has been shown that, in cavities of this size, the Purcell effect plays a minor role.<sup>S24,S25</sup>

### Section S16. Fraction of Absorbed Pump Power

The power of the pump beam absorbed by the gain layer was estimated using the transfer-matrix method described in Ref. S7. The matrix method was applied on the same waveguide structure as used for the multilayer-waveguide model. The reflection and transmission coefficients used for the transfer-matrix method were calculated as described in Ref. S8. For the material parameters, the relative permittivities obtained by ellipsometry were used at the pump free-space wavelength  $\lambda_0 = 405$  nm (see Section S13). For the gain layer, the complex permittivity of the NPL film was employed. The absorbed power was defined as the remaining power after subtracting the reflected power (at the air–gain-layer interface) and the transmitted power (into the Ag layer). Furthermore, the fraction of power incident on the NPL stripe was calculated by integrating a two-dimensional Gaussian over the width ( $2\ \mu\text{m}$ ) and length ( $10\ \mu\text{m}$ ) of the stripe centered to the Gaussian.

### Section S17. Material Gain Estimation for Rate-Equation Model

For the rate-equation model, the material gain as a function of excited carrier number was estimated for a NPL gain layer. A logarithmic model, commonly used to describe gain in semiconductor materials,<sup>S6</sup> was fit to experimental data from Ref. S23:

$$G_{\text{int}}(\langle N \rangle) = G_{\text{int},0} \ln \left( \frac{\langle N \rangle + N_s}{N_{\text{tr}} + N_s} \right). \quad (\text{S7})$$

Here, the intrinsic gain,  $G_i$ , is described as a function of the average carrier number per NPL,  $\langle N \rangle$ . The fit resulted in an empirical intrinsic gain coefficient  $G_{\text{int},0} = 22329\ \text{cm}^{-1}$ , an average transparency carrier number  $N_{\text{tr}} = 4.9$ , and an average shift carrier number  $N_s = 51.8$  [which forces the natural logarithm to be finite for  $\langle N \rangle = 0$ ]. To obtain the material gain, the intrinsic gain was multiplied by the NPL packing fraction, which was taken to be  $f_{\text{pack}} = 40\%$  (Ref. S26). Furthermore, the average carrier number was expressed as the total carrier number,  $N$ , divided by the total number of NPLs,  $N_{\text{NPL}}$ . The total number of NPLs was determined through  $N_{\text{NPL}} = f_{\text{pack}} V_{\text{stripe}} / V_{\text{NPL}}$ , with a stripe volume of  $V_{\text{stripe}} = 10\ \mu\text{m} \times 2\ \mu\text{m} \times d_{\text{NPL}}$  (where  $d_{\text{NPL}}$  is the NPL

stripe thickness) and a NPL volume of  $V_{\text{NPL}} = 22 \text{ nm} \times 22 \text{ nm} \times 10 \text{ nm}$  (estimated from scanning-electron-microscope images). The resulting function for the material gain could then be expressed as:

$$G_{\text{mat}}(N) = G_{\text{int},0} \ln \left( \frac{\frac{N}{N_{\text{NPL}}} + N_s}{N_{\text{tr}} + N_s} \right) f_{\text{pack}}. \quad (\text{S8})$$

## Section S18. Mode-Switching Discussion

Our rate-equation model predicts that metallic-cavity lasers could potentially be employed for switching between photonic and plasmonic lasing at high speeds within the same device. Both the photonic and plasmonic laser pulses evolve on a picosecond to sub-picosecond time scale (Figure 5d). Note that this simplified rate-equation model does not account for the time for carriers to thermalize to the band edge of the NPLs. However, experiments have shown that this thermalization can occur on (sub-)picosecond timescales.<sup>S27,S28</sup> For simultaneous plasmonic and photonic lasing to occur, a gain medium that can provide a material gain of approximately  $3000 \text{ cm}^{-1}$  is required. Even though our NPLs provide sufficient gain for plasmonic lasing for cavities with NPL-stripe thicknesses below the photonic-mode cutoff thickness, the devices with  $d_{\text{NPL}} \geq 74 \text{ nm}$  displayed signs of degradation when the pump fluence was increased far beyond the photonic lasing threshold. We hypothesize that thick gain layers provide a worse heat sink than thin gain layers, and therefore limit the achievable material gain to lower values.

## Section S19. Supplementary References

- (S1) Li, Q.; Liu, Q.; Schaller, R. D.; Lian, T., Reducing the Optical Gain Threshold in Two-Dimensional CdSe Nanoplatelets by the Giant Oscillator Strength Transition Effect. *J. Phys. Chem. Lett.* **2019**, *10*, 1624–1632.
- (S2) Jayanti, S. V.; Park, J. H.; Dejneka, A.; Chvostova, D.; McPeak, K. M.; Chen, X. S.; Oh, S. H.; Norris, D. J., Low-Temperature Enhancement of Plasmonic Performance in Silver Films. *Opt. Mater. Express* **2015**, *5*, 1147–1155.
- (S3) Siegman, A. E., *Lasers*. Univ. Science Books: Mill Valley, 1986.
- (S4) Ning, C. Z., Semiconductor Nanolasers. *Phys. Status Solidi B* **2010**, *247*, 774–788.
- (S5) Hill, M. T.; Gather, M. C., Advances in Small Lasers. *Nat. Photonics* **2014**, *8*, 908–918.
- (S6) Coldren, L. A.; Corzine, S. W.; Mashanovitch, M., *Diode Lasers and Photonic Integrated Circuits*. Wiley: Hoboken, N.J., 2012.
- (S7) Byrnes, S. J., Multilayer Optical Calculations. *arXiv e-prints* **2016**, arXiv:1603.02720.
- (S8) Novotny, L.; Hecht, B., *Principles of Nano-Optics*. 2 ed.; Cambridge University Press: Cambridge, 2012.

- (S9) Sorger, V. J.; Oulton, R. F.; Yao, J.; Bartal, G.; Zhang, X., Plasmonic Fabry-Perot Nanocavity. *Nano Lett.* **2009**, *9*, 3489–3493.
- (S10) Brucoli, G.; Martín-Moreno, L., Effect of Defect Depth on Surface Plasmon Scattering by Subwavelength Surface Defects. *Phys. Rev. B* **2011**, *83*, 075433.
- (S11) Visser, T. D.; Blok, H.; Demeulenaere, B.; Lenstra, D., Confinement Factors and Gain in Optical Amplifiers. *IEEE J. Quantum Elect.* **1997**, *33*, 1763–1766.
- (S12) Robinson, J. T.; Preston, K.; Painter, O.; Lipson, M., First-Principle Derivation of Gain in High-Index-Contrast Waveguides. *Opt. Express* **2008**, *16*, 16659–16669.
- (S13) Ford, G. W.; Weber, W. H., Electromagnetic-Interactions of Molecules with Metal Surfaces. *Phys. Rep.* **1984**, *113*, 195–287.
- (S14) McPeak, K. M.; Jayanti, S. V.; Kress, S. J.; Meyer, S.; Iotti, S.; Rossinelli, A.; Norris, D. J., Plasmonic Films Can Easily Be Better: Rules and Recipes. *ACS Photonics* **2015**, *2*, 326–333.
- (S15) Rossinelli, A. A.; Rojo, H.; Mule, A. S.; Aellen, M.; Cocina, A.; De Leo, E.; Schäublin, R.; Norris, D. J., Compositional Grading for Efficient and Narrowband Emission in CdSe-Based Core/Shell Nanoplatelets. *Chem. Mater.* **2019**, *31*, 9567–9578.
- (S16) Galliker, P.; Schneider, J.; Eghlidi, H.; Kress, S.; Sandoghdar, V.; Poulidakos, D., Direct Printing of Nanostructures by Electrostatic Autofocussing of Ink Nanodroplets. *Nat. Commun.* **2012**, *3*, 1–9.
- (S17) Verhagen, E. Subwavelength Light Confinement with Surface Plasmon Polaritons. PhD Thesis, Utrecht Univ., Utrecht, Netherlands, 2009.
- (S18) Burke, J. J.; Stegeman, G. I.; Tamir, T., Surface-Polariton-Like Waves Guided by Thin, Lossy Metal Films. *Phys. Rev. B* **1986**, *33*, 5186–5201.
- (S19) Landau, L. D.; Lifshitz, E. M.; Bell, J. S.; Kearsley, M. J.; Pitaevskij, L. P.; Sikes, J. B., *Electrodynamics of Continuous Media*. Pergamon Press: Oxford, 1984.
- (S20) Saxena, D.; Mokkapati, S.; Parkinson, P.; Jiang, N.; Gao, Q.; Tan, H. H.; Jagadish, C., Optically Pumped Room-Temperature GaAs Nanowire Lasers. *Nat. Photonics* **2013**, *7*, 963–968.
- (S21) Chen, R.; Tran, T.-T. D.; Ng, K. W.; Ko, W. S.; Chuang, L. C.; Sedgwick, F. G.; Chang-Hasnain, C., Nanolasers Grown on Silicon. *Nat. Photonics* **2011**, *5*, 170–175.
- (S22) Antolinez, F. V.; Rabouw, F. T.; Rossinelli, A. A.; Keitel, R. C.; Cocina, A.; Becker, M. A.; Norris, D. J., Trion Emission Dominates the Low-Temperature Photoluminescence of CdSe Nanoplatelets. *Nano Lett.* **2020**, *20*, 5814–5820.
- (S23) Geiregat, P.; Tomar, R.; Chen, K.; Singh, S.; Hodgkiss, J. M.; Hens, Z., Thermodynamic Equilibrium between Excitons and Excitonic Molecules Dictates Optical Gain in Colloidal CdSe Quantum Wells. *J. Phys. Chem. Lett.* **2019**, *10*, 3637–3644.
- (S24) Kress, S. J. P.; Cui, J.; Rohner, P.; Kim, D. K.; Antolinez, F. V.; Zaininger, K. A.; Jayanti, S. V.; Richner, P.; McPeak, K. M.; Poulidakos, D.; Norris, D. J., A Customizable Class of Colloidal-Quantum-Dot Spasers and Plasmonic Amplifiers. *Sci. Adv.* **2017**, *3*, e1700688.
- (S25) Khurgin, J. B.; Noginov, M. A., How Do the Purcell Factor, the Q-factor, and the Beta Factor Affect the Laser Threshold? *Laser Photonics Rev.* **2021**, 2000250.

- (S26) Tomar, R.; Kulkarni, A.; Chen, K.; Singh, S.; van Thourhout, D.; Hodgkiss, J. M.; Siebbeles, L. D. A.; Hens, Z.; Geiregat, P., Charge Carrier Cooling Bottleneck Opens up Nonexcitonic Gain Mechanisms in Colloidal CdSe Quantum Wells. *J. Phys. Chem. C* **2019**, *123*, 9640–9650.
- (S27) Pelton, M.; Ithurria, S.; Schaller, R. D.; Dolzhenkov, D. S.; Talapin, D. V., Carrier Cooling in Colloidal Quantum Wells. *Nano Lett.* **2012**, *12*, 6158–6163.
- (S28) Sippel, P.; Albrecht, W.; van der Bok, J. C.; Van Dijk-Moes, R. J.; Hannappel, T.; Eichberger, R.; Vanmaekelbergh, D., Femtosecond Cooling of Hot Electrons in CdSe Quantum-Well Platelets. *Nano Lett.* **2015**, *15*, 2409–2416.